

Analytical Magnetic Model for Variable-Flux Interior Permanent Magnet Synchronous Motors

Wang, Bingnan; Shin, Kyung-Hun; Hidaka, Yuki; Kondo, Shota; Arita, Hideaki; Ito, Kazumasa

TR2021-123 October 20, 2021

Abstract

In this paper, we present a new semi-analytical magnetic modeling method for a variable-flux interior permanent magnet synchronous motor (IPMSM), which features both permanent magnets and field windings in the rotor. Developed on subdomain framework, we account for all the excitation sources, the finite permeability of rotor core, and the stator slotting effect in the calculation to obtain key electromagnetic performance metrics, such as back-EMF and torque. The calculation is validated with high-fidelity finite-element simulations and experimental results from a prototype motor. The method can achieve good accuracy with rapid calculation, making it suitable for motor design optimization.

IEEE Energy Conversion Congress and Exposition (ECCE) 2021

Analytical Magnetic Model for Variable-Flux Interior Permanent Magnet Synchronous Motors

Bingnan Wang¹, Kyung-Hun Shin¹, Yuki Hidaka², Shota Kondo², Hideaki Arita², and Kazumasa Ito²

¹ Mitsubishi Electric Research Laboratories, 201 Broadway, Cambridge, MA 02139, USA

² Advanced Technology R&D center, Mitsubishi Electric Corporation, 8-1-1, Tsukaguchi-Honmachi, Amagasaki, Hyougo, Japan
bwang@merl.com

Abstract—In this paper, we present a new semi-analytical magnetic modeling method for a variable-flux interior permanent magnet synchronous motor (IPMSM), which features both permanent magnets and field windings in the rotor. Developed on subdomain framework, we account for all the excitation sources in the machine, the finite permeability of rotor core, and the stator slotting effect in the calculation to obtain key electromagnetic performance metrics, such as air-gap flux density, back-EMF and torque. The calculation is validated with high-fidelity finite-element simulations and experimental results from a prototype motor. The method is shown to achieve good accuracy with rapid calculation, making it suitable for motor design optimization.

Index Terms—Interior permanent magnet motor, variable-flux, magnetic field modeling, subdomain method

I. INTRODUCTION

Interior permanent magnet synchronous motors (IPMSMs) have been widely used in various industrial applications, due to many advantages such as high torque, high power density, and high efficiency [1], [2]. With the use of rare-earth permanent magnets, high magnetic flux linkage can be achieved without additional copper loss, and high efficiency and power density can hence be realized. However, the magnetic flux density provided by the magnets is fixed, and there is often a mismatch between the high efficiency region and frequently operated regions of an IPMSM. Indeed, at low torque condition, lower magnetic flux density is actually preferred in order to reduce the iron loss. Lower magnetic flux density also helps suppress induced voltage especially during high speed operation. Therefore field weakening is a commonly used control strategy for IPMSM. However, the high field weakening current required for such operation introduces more copper loss, and lowers the efficiency of the machine. In order to extend the high efficiency range of IPMSMs, variable-flux permanent magnet machines have been proposed with the capability to tune the magnetic flux while maintaining a high efficiency, especially at field weakening conditions, including mechanically adjusted motors [3], memory motors [4], and hybrid excitation motors [5]–[8]. In particular, hybrid excitation IPMSMs with DC field windings in the rotor have recently been investigated theoretically and experimentally [6], [8] due to their flux tuning capability with both field strengthening and field weakening operation. It has been shown in Ref. [8] that up to 47.1% copper loss reduction can be achieved with the proposed variable-flux IPMSM with field windings, due to the

significant reduction of field weakening stator current at high speed.

Due to the more complex topology and magnetic flux path, the magnetic field modeling and analysis is especially important for these novel machines. Finite-element method (FEM) based simulations are important tools for researchers and motor designers. While highly accurate, they are also very time-consuming and computation-intensive, and not the best choice for quick screening of many design candidates or optimizing many design parameters. On the other hand, analytical modeling methods, such as relative permeance method, complex permeance method, and subdomain method [9], [10], can be complimentary to FEM with fast calculation speed and reasonable accuracy. These methods formulate the problem into a single partial differential equation (PDE) of a magnetic potential derived from Maxwell's equations, and solve for the PDE to find closed-form solutions. While permeance models adopt the same air gap permeance function for any rotor position to account for the slotting effect, subdomain method evaluates the influence of slotting for each rotor position, making it more accurate than permeance method [11]. Most of the developed analytical methods have been focusing on the air gap field modeling of surface-mounted permanent magnet (SMPM) machines and switched reluctance machines [12], [13] due to the relatively simple topology. IPMSMs on the other hand, have more complex rotor structures with embedded PMs and more challenging to describe analytically, and the subdomain based analytical methods were not developed until recently [14], [15].

This paper presents for the first time, to the best of our knowledge, a subdomain method for the analytical calculation of magnetic fields in a variable-flux IPMSM, where both PMs and separately excited field windings are embedded in the rotor. The method deals with all excitation sources in the calculation, and takes slotting effect into consideration, and is capable of calculating both open-circuit and on-load fields. The finite permeability of different regions of the rotor core is also included in the calculation to account for the saturation effect of corresponding regions. The calculation results are validated with both FEM simulations and experimental measurements of a prototype motor.

The rest of the paper is organized as follows. In Section II, we introduce the design of the variable-flux motor and

the detailed modeling process; in Section III, we present the calculation results and compare against the FEM simulations and experimental measurements, discussions on the accuracy and potential use cases of the proposed method will also be provided; a summary of the paper will be given in Section IV.

II. THE PROPOSED METHOD

In this section, we first introduce the principle and design of the variable-flux IPMSM, and then lay out the proposed analytical calculation process for the analysis of the machine.

A. Variable-Flux IPMSM Design

In this work, a 48-slot 8-pole variable-flux IPMSM is designed and analyzed. The motor rotor and stator structures are shown in Fig. 1(a) and Fig. 1(b) respectively, and major geometrical parameters are shown in Table I. As shown in Fig. 1(a), the rotor of the variable-flux IPMSM is composed of the laminated rotor core and 8 field winding units, which are fabricated separately before assembled together with the laminated core. Each of the field winding unit consists of a piece of permanent magnet, a small block of laminated iron core, and a field winding made of 28 turns of copper wires. The assembled field winding units are inserted into the slots of the laminated rotor core and fixed with adhesive bonding. Brush and slip ring are used to supply DC current to the field windings. This manufacturing method makes the winding process easier, and ensures good mechanical strength of the machine during high speed operation. For stator winding, two rectangular copper wires are filled in each of the 48 slots, and 6-phase distributed winding is configured.

TABLE I: Motor Parameters

Parameter	Value
Stator outer diameter (mm)	138.0
Stator inner diameter (mm)	95.4
Stator slot number	48
Winding turns per slot	2
Number of phases	6
Rotor outer diameter (mm)	94.4
Rotor inner diameter (mm)	37
Rotor pole number	8
Field winding turns	28
Stack length (mm)	100
Magnet remnant flux density (T)	1.30

With the proposed variable-flux motor, it is possible to actively control the rotor flux with either field strengthening or field weakening through the excitation of the field windings. It is shown in Ref. [8] that up to 47.1% copper loss reduction can be achieved with the proposed motor due to the reduction of field weakening stator current at high speed of 20,000 rpm under a small 5 N·m load.

B. The Modeling Process

In the analytical model, we solve for the PDE of magnetic vector potential that is derived from the Maxwell's equations

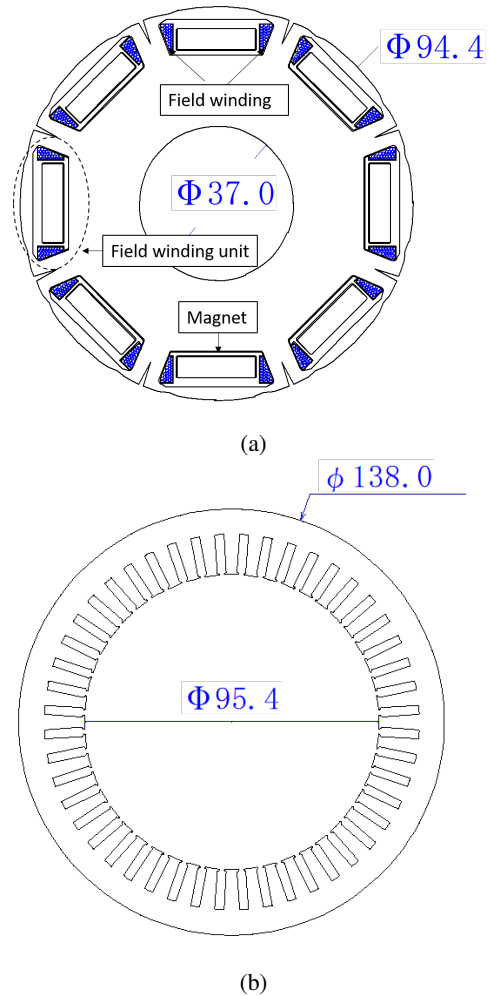


Fig. 1: The cross-section view of the variable-flux IPMSM structure: (a) rotor and (b) stator. Dimensions are in mm.

under magneto-static approximation. To be able to obtain analytical closed-form solutions, the physical structure of the variable-flux motor is simplified in 2D polar coordinates. For the calculation process, we divide the structures into separate regions, or subdomains depending on the materials and excitation sources; then the governing PDE of each region is written respectively, with general solutions calculated and described analytically; next boundary conditions between neighboring regions are set up in order to fully identify the unknown coefficients in the general solutions. The electromagnetic performances can be calculated subsequently using vector potential solutions.

In order to be able to solve for the magnetic vector potentials analytically, a few simplifications and assumptions are applied to the motor topology: the end effect in axial direction is neglected, therefore the problem is reduced to 2d; the motor structures are further simplified so that they can be described in 2d polar coordinate with radial sides, including the stator slots and openings, permanent magnets and DC field windings. Fig. 2(a) shows the simplified geometry of the variable-flux

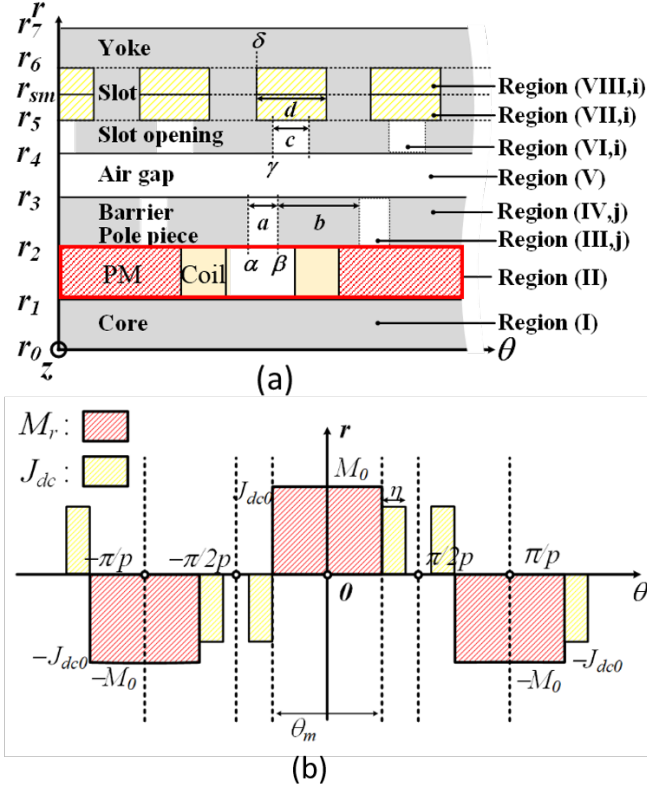


Fig. 2: (a) The subdomains for the analytical model of the variable-flux IPMSM. (b) The distribution of excitation sources in Region II, including PM magnetization and field winding current density, as a function of rotor angle.

IPMSM in the polar coordinate, with subdomains labelled respectively: Region I represent the rotor yoke, Region II represent the PM and field winding, Regions III and IV represent rotor barriers and pole-pieces, Regions VI represents the slot-openings, Regions VII and VIII represent the two-layer stator windings in the slots, and Region V is the air-gap. Different permeability values are assigned to the rotor

$$A_z^{II}(r, \theta) = A_o^{II} + B_o^{II} \ln r + \sum_{n=1}^{\infty} \left[\begin{aligned} & (A_n^{II} r^{-n} + B_n^{II} r^n + (W_n^m(r) + W_n^j(r)) \cos n\theta_o) \sin n\theta \\ & + (C_n^{II} r^{-n} + D_n^{II} r^n - (W_n^m(r) + W_n^j(r)) \sin n\theta_o) \cos n\theta \end{aligned} \right] \quad (6)$$

where the contribution from PM magnetization is

$$W_n^m(r) = \begin{cases} \frac{r \mu_0 n}{((n)^2 - 1)} M_n, & n/p = 1, 3, 5... \\ \frac{\mu_0}{2} r \ln r M_n, & np = 1 \\ 0, & \text{otherwise} \end{cases}, \quad (7)$$

core domains to account for the saturation effect of the ferromagnetic material. Regions I, II, and V have periodic shapes and are homogeneous in the tangential direction.

Depending on whether there is a magnetic source in the subdomain, the governing equation for the magnetic vector potential, which is defined as $\nabla \times \mathbf{A} = \mathbf{B}$, can be written as either a Poisson's equation or Laplace's equation. Specifically for region II, where both PM and field winding exist, the governing equation is written as

$$\nabla^2 \mathbf{A}_z^{II} = -\mu_0 (\mathbf{J}_{dc} + \nabla \times \mathbf{M}) \quad (1)$$

where \mathbf{J}_{dc} is the field winding current density, and \mathbf{M} is the magnetization of the PM. Their distribution as function of rotor angle θ is shown in Fig. 2(b). They can be expanded into two separate Fourier series. The magnetization of the permanent magnets is in radial direction and is expanded as

$$M(\theta) = \sum_{n=1,3,5,\dots}^{\infty} M_n \cos [n(\theta - \theta_o)] \quad (2)$$

with the corresponding Fourier coefficients

$$M_n = \frac{4M_o}{n\pi} \sin\left(\frac{n\pi\alpha}{2}\right) \cos[n(\theta - \theta_o)], \quad (3)$$

where α is the pole-to-arc ratio of the magnet, and θ_o is the initial rotor angle. Similarly the field winding current density is expanded as

$$J_{dc} = \sum_{n=1,3,5,\dots}^{\infty} J_{dcn} \sin [n(\theta - \theta_o)] \quad (4)$$

with the corresponding Fourier coefficients

$$J_{dcn} = \frac{4J_{dcn0}}{n\pi} \left[\sin\left(\frac{n\pi\alpha + 2p\eta}{2}\right) - \sin\left(\frac{n\pi\alpha}{2}\right) \right] \quad (5)$$

where η is the angular span of the DC field winding.

Subsequently the solution for (1) can be derived using superposition principle, as the summations of the general solution of the corresponding Laplace's equation without the source terms, and the particular solutions due to the two source terms.

and the contribution from the field winding current density is

$$W_n^j(r) = \begin{cases} \frac{\mu_0 J_{dcn}}{(n^2 - 4)} r^2, & n/p = 1, 3, 5... \\ \frac{\mu_0}{4} r^2 J_{dcn} \left(\frac{1}{4} - \ln r\right), & np = 2 \\ 0, & \text{otherwise} \end{cases} \quad (8)$$

where M_n and J_{dcn} are the n -th Fourier component of the magnetization M and field winding current density J_{dc} , and are given in equations (3) and (5), respectively.

The governing equations and their solutions for other subdomains can be derived in a similar manner. Special attention needs to be given to non-periodic subdomains such as rotor

bridges and pole pieces, where separate Fourier series needs to be defined to account for the angular dependence of the subdomains.

For non-periodic subdomains without source terms (domains III and IV), the magnetic vector potential is governed by Laplace's equation $\nabla^2 \mathbf{A} = 0$, and the general solution can be expressed as the superposition of Fourier series:

$$A_z(r, \theta) = A_0 + B_0 \ln r + \sum_{k=1}^{\infty} \left(A_k (r)^{-k} + B_k (r)^k \right) \cos(k(\theta - \theta_1)) + \sum_{m=1}^{\infty} \left(A_m \frac{\sinh(k_m(\theta - \theta_1))}{\sinh(k_m \zeta)} + B_m \frac{\sinh(k_m(\theta - \theta_2))}{\sinh(k_m \zeta)} \right) \sin \left[k_m \ln \left(\frac{r}{r_i} \right) \right] \quad (9)$$

where k and m are integers representing harmonic orders, $k_k = k\pi/\zeta$, $k_m = m\pi/\ln(r_o/r_i)$, with r_i and r_o the inner and outer radii of the subdomain respectively, ζ is the angular width of the subdomain, θ_1 and θ_2 are the beginning and ending angular positions of the subdomain, respectively.

For the air gap domain V, the solution to the governing Laplace's equation takes the form of

$$A_z^V(r, \theta) = A_0^V + B_0^V \ln r + \sum_{n=1}^{\infty} \left(A_n^V \left(\frac{r}{r_3} \right)^{-n} + B_n^V \left(\frac{r}{r_4} \right)^n \right) \sin n\theta + \sum_{n=1}^{\infty} \left(C_n^V \left(\frac{r}{r_3} \right)^{-n} + D_n^V \left(\frac{r}{r_4} \right)^n \right) \cos n\theta \quad (10)$$

For slot opening domain VI, the solution is express as

$$A_z^{VI,i}(r, \theta) = A_0^{VI,i} + B_0^{VI,i} \ln r + \sum_{k=1}^{\infty} \left(A_k^{VI,i} \left(\frac{r}{r_4} \right)^{-k} + B_k^{VI,i} \left(\frac{r}{r_5} \right)^k \right) \cos[k_{kc}(\theta - \gamma_i)] \quad (11)$$

where i represents the i -th slot opening, and γ represents the starting angular position of the slot opening, and $k_{kc} = k\pi/c$ with c the angular width of the slot opening.

For slot regions, the vector potential is governed by Poisson's equation of the form $\nabla^2 \mathbf{A} = -\mu_0 \mathbf{J}$, where \mathbf{J} is the surface current density in the region. For domain VII, the solution of vector potential is obtained as

$$A_z^{VII,i}(r, \theta) = A_0^{VII,i} + B_0^{VII,i} \ln r - \mu_0 J_z^{VII,i} r^2 / 4 + \sum_{v=1}^{\infty} \left(A_v^{VII,i} \left(\frac{r}{r_5} \right)^{-v} + B_v^{VII,i} \left(\frac{r}{r_{sm}} \right)^v \right) \cos[k_{vd}(\theta - \delta_i)] \quad (12)$$

where i represents the i -th slot, and δ represents the starting angular position of the slot opening, and $k_{vd} = v\pi/d$ with d the angular width of the slot. The solution for domain VIII can be expressed similarly.

Once closed-form solutions for all subdomains are obtained, the next step in the calculation is to apply proper boundary conditions to neighboring subdomains, in order to fully determine the unknown coefficients in the solutions. For non-periodic subdomains, non-homogeneous boundary conditions in both radial and tangential directions need to be defined to obtain all the unknown coefficients. The continuity of the magnetic field at the boundary between domains χ and $\chi + 1$ can be expressed as

$$\mathbf{n} \cdot (\mathbf{B}^{(\chi)} - \mathbf{B}^{(\chi+1)}) = 0 \quad (13)$$

$$\mathbf{n} \times (\mathbf{H}^{(\chi)} - \mathbf{H}^{(\chi+1)}) = \mathbf{J}_s \quad (14)$$

where J_s is the current density on the boundary, and n is the unity vector normal to that boundary. The continuity of the normal component of the magnetic flux density (13) can be mathematically simplified as the continuity of the magnetic vector potential [9]. A system of linear equations can be set up from these boundary conditions, and the full solution of magnetic potential can be obtained after solving for the equations.

The electromagnetic performance metrics, such as magnetic flux density, flux linkage, induced voltage, and torque waveform, can be calculated subsequently. In particular, the magnetic flux density components in the radial direction B_r and tangential direction B_θ can be directly obtained from the magnetic vector potential, according to its definition:

$$\mathbf{B}_r = \frac{1}{r} \frac{\partial A_z}{\partial \theta} \mathbf{i}_r, \quad \mathbf{B}_\theta = -\frac{\partial A_z}{\partial r} \mathbf{i}_\theta \quad (15)$$

The flux linkage associated with each stator slot can be obtained from vector potential using Stokes' theorem:

$$\phi = \int_S \mathbf{B} dS = \oint_l \mathbf{A} dl, \quad (16)$$

where S is the surface of the slot, and l is its boundary, and the total flux linkage of each phase is calculated by summing all contributions from the phase winding. The back-EMF is then obtained with $E_a = -d\phi/dt$. The torque is calculated from the air gap flux using Maxwell stress tensor

$$T = \frac{l_k r^2}{\mu_0} \int_0^{2\pi} B_{rg} B_{\theta g} d\theta = \frac{l_k r^2}{\mu_0} \sum_{n=1}^N (B_{rc} B_{\theta c} + B_{rs} B_{\theta s}), \quad (17)$$

where r is the radius of the air gap, B_{rg} and $B_{\theta g}$ are the radial and tangential flux density in the air gap, respectively, and the subscripts c and s denote the cosine and sine components of the flux harmonics, respectively.

III. RESULTS & DISCUSSIONS

The calculation method proposed in the previous session is implemented and compared with FEM simulations. Fig. 3 shows the comparison of the actual geometry of the machine and the simplified geometry for the analytical calculation. All the major parameters of the motor listed in Table I apply to the analytical model as well. Additional parameters for the analytical model geometry are listed in Table II. Note that

due to the simplification of the motor topology under polar coordinates, several structures have to be modified: the shapes of the magnets and the DC field winding slots are modified to be described in one subdomain under polar coordinate; small features on the rotor surfaces serving as flux barriers are neglected and a smooth rotor surface is assumed instead; the slot opening shape is simplified; the rectangular slots are modified to have radial sides.

With the parameters shown in Table I and Table II, we construct the analytical model using the process presented in the previous section, solve for the magnetic vector potentials of the motor, and calculate subsequently the motor performances. To achieve good precision in the analytical evaluation, the number of harmonic orders included in the computations are $N = 100$, which accounts for the harmonics in the air-gap and PM subdomains, $V = M = K = 7$, which account for the harmonics in the barrier, pole-piece, slots, and slot-opening subdomains. Fig. 4 shows the calculated radial air gap flux density distribution at no-load condition, with DC current in the field windings to be 10 A. The analytical result agrees well with FEM except the small features around the edges of the peaks. This is due to the simplification of the structures around the field winding unit and the flux barrier around the rotor surface when setting up the subdomains. Therefore the flux path in the analytical model, especially for the leakage flux of the magnet, is not exactly the same as the actual machine.

TABLE II: Geometrical Parameters of the Analytical Model

Parameter	Value
Slot height (mm)	11.4
Ratio of slot width to slot pitch	0.36
Slot opening height (mm)	1
Ratio of slot opening width to slot pitch	0.24
Air gap length (mm)	0.5
Permanent magnet height (mm)	5
Ratio of permanent magnet width to pole pitch	0.65
Ratio of DC winding width to pole pitch	0.055
Ratio of pole piece width to pole pitch	0.76
Pole piece height (mm)	4

A prototype of the variable-flux IPM motor has been built and tested, with a photo of assembled rotor including the fielding winding units shown in Fig. 5(a) and the test bench shown in Fig. 5. For on-load test, a second motor is connected to the prototype motor via shaft to serve as load, and the torque produced by the prototype motor to drive the load is measured using a torque meter.

As part of the comparative study, the line-to-line back-EMF at no-load condition is calculated with the proposed method, simulated using FEM, and measured using the prototype motor at the speed of 1000 rpm, and the result is shown in Fig. 6. While the analytical calculation result is in good agreement with FEM and experiment measurement, the waveform differs. This is again due to the simplification of the flux barrier and winding unit structure in the analytical model, making the flux path different from the actual motor. Therefore at

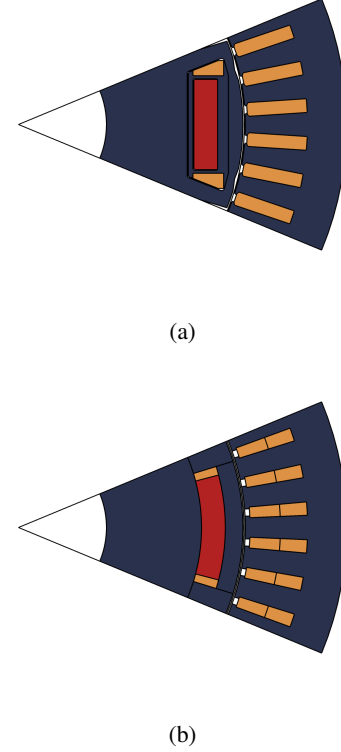


Fig. 3: The comparison of (a) the actual geometry and (b) the simplified geometry for the analytical model. One eighth of the cross section is plotted.

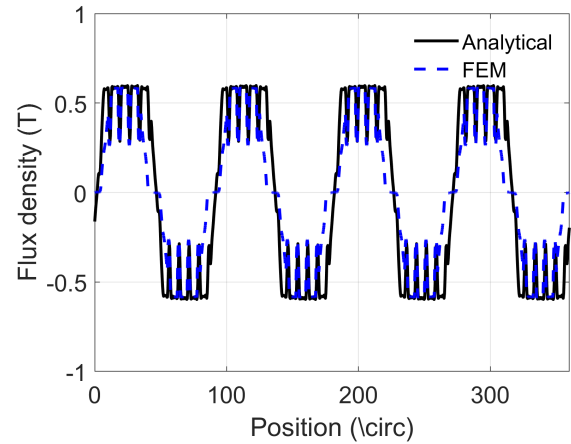
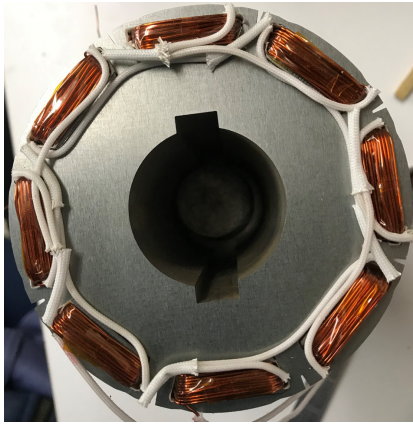


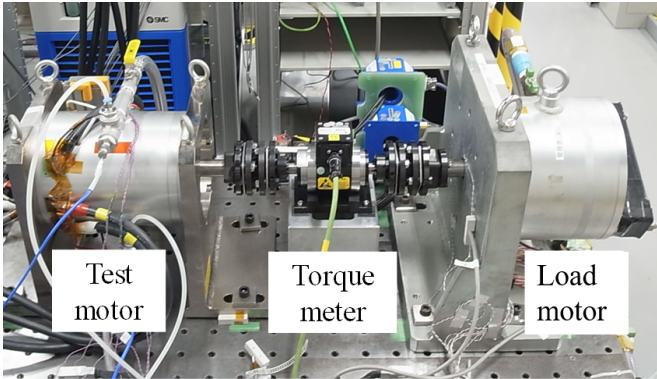
Fig. 4: The calculated radial air gap flux density distribution at open circuit condition, compared with FEM simulation result. DC current is 10 A in field windings.

each time instance, the flux distribution differs, causing the difference integrated flux linkage and the induced voltage in stator windings.

For on-load test, we apply 250 Arms phase current in the stator windings, and measure the torque generation of the motor at different current angles. Different excitation



(a)



(b)

Fig. 5: (a) The fabricated rotor assembly of the motor including the field winding units, and (b) the fully assembled prototype motor and the test bench.

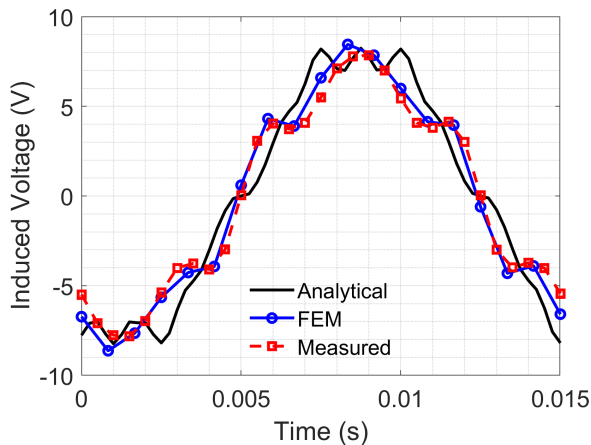
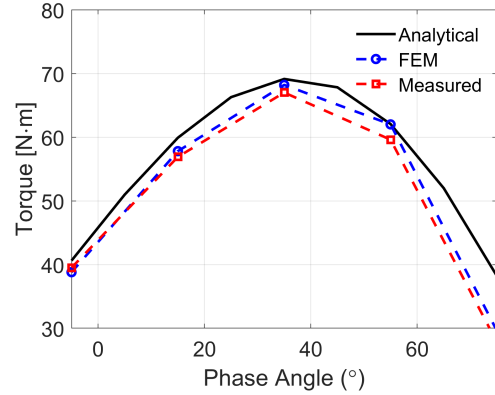


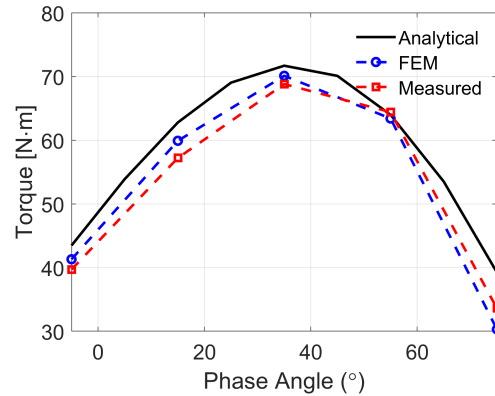
Fig. 6: The calculated line-to-line back-EMF at 1000 rpm, plotted with FEM simulation and experiment result. DC current is 10 A in field windings.

conditions for the DC field windings were tested, and the results for 0 and 10 A DC current are shown in Fig. 7 (a) and Fig. 7(b), respectively. For both cases, the analytical

result is slightly higher than the measured and FEM results, which is largely due to the overestimation of the air gap flux and induced voltage caused by geometry simplification in the analytical model. Furthermore, torque increase due to the excitation current in the DC field windings is observed for both analytical and experiment results.



(a)



(b)

Fig. 7: The comparison of analytical, FEM, and experiment of on-load torque generation of the motor as a function of current phase angle, with 250 Arms phase current (a) with no field winding excitation, and (b) with 10 A DC current in field windings.

It is worth to note that, for a given rotor position, the computation time is less than 1 second with the analytical model, whereas the nonlinear FEM analysis takes approximately 30 seconds with 47,263 elements included in the simulation model. Therefore, the proposed calculation method can achieve good calculation accuracy with a small fraction of time of FE simulations, making it more suitable to quickly evaluate the performances of a large amount of motor design candidates, conduct parameter sweeping, and adopt into an optimization routine to identify the optimal motor design.

Due to the relatively complicated topology of the variable-flux IPM motor, we did observe some mismatch in the calculation results of the analytical model, such as the air-gap magnetic flux density distribution, the waveform of the back-

EMF, due to the unavoidable simplification of the geometry in order to be able to obtain closed-form solutions for the magnetic vector potential. Therefore, we envision the proposed method to be applied complimentary to FEM simulations for motor design optimization, with the analytical model used for preliminary design parameter selection and optimization for major design parameters, such as the slot and pole numbers, size of the slots and magnets, while the FEM simulations can be used for fine tuning of the detailed geometries, such as the shape of rotor flux barriers and the the slot opening. With such combined design approach, we can reduce the number of FEM simulation required, and reduce the overall design time frame.

IV. CONCLUSIONS

In this paper, we developed a subdomain based semi-analytical modeling technique for a variable-flux interior permanent magnet synchronous motor. Multiple excitation sources, including the stator windings, the permanent magnets, the DC field windings, can be modelled for both open-circuit and on-load field calculations. The air gap magnetic flux, back-EMF and torque generation were calculated and compared with finite-element simulations and experiment measurements on a prototype motor. The calculation result using the proposed method agrees well while uses much less time to solve than finite-element simulation.

REFERENCES

- [1] S. Morimoto, "Trend of permanent magnet synchronous machines," *IEEE Transactions on Electrical and Electronic Engineering*, vol. 2, no. 2, pp. 101–108, 2007. [Online]. Available: <https://onlinelibrary.wiley.com/doi/abs/10.1002/tee.20116>
- [2] G. Pellegrino, A. Vagati, P. Guglielmi, and B. Boazzo, "Performance comparison between surface-mounted and interior pm motor drives for electric vehicle application," *IEEE Transactions on Industrial Electronics*, vol. 59, no. 2, pp. 803–811, 2012.
- [3] R. Owen, Z. Q. Zhu, J. B. Wang, D. A. Stone, and I. Urquhart, "Mechanically adjusted variable-flux concept for switched-flux permanent-magnet machines," in *2011 International Conference on Electrical Machines and Systems*, 2011, pp. 1–6.
- [4] V. Ostovic, "Memory motors-a new class of controllable flux pm machines for a true wide speed operation," in *Conference Record of the 2001 IEEE Industry Applications Conference. 36th IAS Annual Meeting (Cat. No.01CH37248)*, vol. 4, 2001, pp. 2577–2584 vol.4.
- [5] T. Kato, M. Minowa, H. Hijikata, K. Akatsu, and R. D. Lorenz, "Design methodology for variable leakage flux ipm for automobile traction drives," *IEEE Transactions on Industry Applications*, vol. 51, no. 5, pp. 3811–3821, 2015.
- [6] T. Kosaka, M. Sridharbabu, M. Yamamoto, and N. Matsui, "Design studies on hybrid excitation motor for main spindle drive in machine tools," *IEEE Transactions on Industrial Electronics*, vol. 57, no. 11, pp. 3807–3813, 2010.
- [7] T. Takahashi, M. Takemoto, S. Ogasawara, T. Ogawa, H. Arita, and A. Daikoku, "Development of a consequent pole pm type axial-gap motor with dc field winding," in *2019 IEEE International Electric Machines Drives Conference (IEMDC)*, 2019, pp. 766–773.
- [8] Y. Hidaka, S. Fujikura, S. Kondo, H. Arita, and M. Iezawa, "A novel variable flux permanent magnet synchronous motor with separately excited field winding," in *2020 23th International Conference on Electrical Machines and Systems (ICEMS)*, 2020, pp. 1–4.
- [9] B. L. J. Gysen, K. J. Meessen, J. J. H. Paulides, and E. A. Lomonova, "General formulation of the electromagnetic field distribution in machines and devices using fourier analysis," *IEEE Transactions on Magnetics*, vol. 46, no. 1, pp. 39–52, 2010.
- [10] L. J. Wu, Z. Q. Zhu, D. A. Staton, M. Popescu, and D. Hawkins, "Comparison of analytical models of cogging torque in surface-mounted pm machines," *IEEE Transactions on Industrial Electronics*, vol. 59, no. 6, pp. 2414–2425, 2012.
- [11] B. Hannon, P. Sergeant, L. Dupré, and P. Pfister, "Two-dimensional fourier-based modeling of electric machines—an overview," *IEEE Transactions on Magnetics*, vol. 55, no. 10, pp. 1–17, 2019.
- [12] Z. Q. Zhu and D. Howe, "Instantaneous magnetic field distribution in brushless permanent magnet dc motors. iii. effect of stator slotting," *IEEE Transactions on Magnetics*, vol. 29, no. 1, pp. 143–151, 1993.
- [13] Z. Q. Zhu, L. J. Wu, and Z. P. Xia, "An accurate subdomain model for magnetic field computation in slotted surface-mounted permanent-magnet machines," *IEEE Transactions on Magnetics*, vol. 46, no. 4, pp. 1100–1115, 2010.
- [14] K.-H. Shin, H.-I. Park, H.-W. Cho, and J.-Y. Choi, "Analytical prediction for electromagnetic performance of interior permanent magnet machines based on subdomain model," *AIP Advances*, vol. 7, p. 056669, 05 2017.
- [15] K. Shin and B. Wang, "Semi-analytical modeling for interior permanent magnet synchronous machines considering permeability of rotor core," in *2020 23th International Conference on Electrical Machines and Systems (ICEMS)*, 2020, pp. 1–4.